Elemental redistributions at structural defects in $Cu(In,Ga)Se_2$ thin films for solar cells

Cite as: J. Appl. Phys. **120**, 205301 (2016); https://doi.org/10.1063/1.4967731
Submitted: 17 August 2016 . Accepted: 26 October 2016 . Published Online: 22 November 2016

E. Simsek Sanli, Q. M. Ramasse, W. Sigle, D. Abou-Ras, R. Mainz, A. Weber, H.-J. Kleebe, and P. A. van Aken

Elemental redistributions at structural defects in Cu(In,Ga)Se_2 thin films for solar cells

E. Simsek Sanli,[1,a)] Q. M. Ramasse,[2] W. Sigle,[1] D. Abou-Ras,[3] R. Mainz,[3] A. Weber,[3] H.-J. Kleebe,[4] and P. A. van Aken[1]
[1]*Stuttgart Center for Electron Microscopy, Max Planck Institute for Solid State Research, Heisenbergstr. 1, Stuttgart 70569, Germany*
[2]*SuperSTEM Laboratory, SciTech Daresbury Campus, Daresbury, Keckwick Lane WA4 4AD, United Kingdom*
[3]*Helmholtz-Zentrum Berlin für Materialien und Energie GmbH, Hahn-Meitner-Platz 1, Berlin 14109, Germany*
[4]*Institut für Angewandte Geowissenschaften, Technische Universität Darmstadt, Schnittspahnstr. 9, Darmstadt 64287, Germany*

(Received 17 August 2016; accepted 26 October 2016; published online 22 November 2016)

The microstructural evolution of Cu(In,Ga)Se_2 absorber layers during a three-stage-type co-evaporation process was studied to elucidate the effect of a Cu-rich stage on the formation of extended structural defects. Defect densities for two Cu-poor samples, one interrupted before and one after this crucial Cu-rich composition stage, were investigated by scanning transmission electron microscopy (STEM) imaging. The structure and chemical nature of individual defects were investigated by aberration-corrected high-resolution STEM in combination with electron energy-loss spectroscopy on the atomic-scale. In spite of the different defect densities between the two samples, most of the individual defects exhibited similar chemistry. In particular, the elemental distributions of atomic columns at {112} twin planes, which are very frequent in Cu(In,Ga)Se_2 thin films, were found to be the same as in the defect-free grain interiors. In contrast, within grain boundaries, dislocation cores, and other structurally more complex defects, elemental redistributions of Cu and In were observed.
[http://dx.doi.org/10.1063/1.4967731]

I. INTRODUCTION

Cu(In,Ga)Se_2 (CIGSe) based thin-film solar cells hold great technological potential thanks to their high absorption coefficients, tunable band-gap energies, and high power conversion efficiencies of up to 22.6%.[1] In order to further enhance the efficiency of these devices, it is necessary to control the microstructure by understanding the microstructural evolution during their fabrication process. It is well known that during CIGSe film deposition by co-evaporation, the microstructure strongly changes when the composition is changed from Cu-poor ([Cu] < ([In] + [Ga])) to Cu-rich ([Cu] > ([In] + [Ga])), resulting in larger grain sizes.[2] It has been speculated that a recrystallization taking place at this process step might—besides a reduction of grain boundaries (GBs)—also lead to a reduction of detrimental defects inside the grains,[3,4] finally leading to higher solar cell efficiencies.[5]

Interruption of CIGSe co-evaporation processes at different stages has allowed intensive analysis of this microstructural evolution. This approach has already been used for investigating the recrystallization at the Cu-poor to Cu-rich transition during co-evaporation, for shedding light on grain boundary (GB) motion and defect annihilation, and for understanding the origin of secondary-phase formations in the CIGSe thin films.[3,5–10] Yan *et al.*[9] revealed differences in the structure and chemistry of the CIGSe layer by changing from Cu-rich to In-rich compositions. They demonstrated the formation of a secondary phase, $Cu_{2-x}Se$, on the sample surface during the early growth stages and its disappearance at the In-rich stage. Furthermore, they showed a correlation between the Cu amount and grain size. In several other studies, linear (dislocations) and planar defects (twin boundaries—TBs, stacking faults—SFs, and random GBs) have been analyzed by microscopic and simulation techniques.[11–15] The formation mechanisms and effects of linear and planar defects have been investigated for individual defects. Recently, Abou-Ras *et al.* discussed varied behavior of atomic reconstructions at the GBs and their possible effects on the absorber layer.[14] Mirhoisseini *et al.* showed that cation-Se-terminated TBs do not affect electronic properties.[15] Nevertheless, a detailed study revealing the cation distributions of several structural defects at the atomic scale has not been published yet.

In the present work, we studied two Cu-poor CIGSe thin films produced at low temperatures (430 °C) in the same chamber, one of them being simply removed at an earlier stage during the fabrication process. We first analyzed the density of defects by means of low-angle annular dark-field (LAADF) imaging in scanning transmission electron microscopy (STEM).[16] We found a number of defects of various types which were not annihilated completely after going through the full evaporation process. Therefore, we give an atomically resolved insight about the structure and chemistry

[a)]Author to whom correspondence should be addressed. Electronic mail: e.simsek@fkf.mpg.de

of linear and planar defects present in the absorber before and after the crucial Cu-rich stage of the fabrication by high-resolution high-angle annular dark-field (HAADF) imaging and electron energy-loss spectroscopy (EELS). The present work provides a comparison of the defects present in the growth-interrupted sample and the defects remaining in the finished sample, and probes the structural and compositional changes at individual defects in order to shed light on their possible influence on device performance.

II. MATERIALS AND METHODS

Two CIGSe absorber layers were grown by a three-stage-type co-evaporation process on a Mo-coated soda-lime glass (SLG).[17] The SLG had a SiN layer as a Na barrier to prevent Na diffusion into the absorber layer. The three-stage-type co-evaporation process, summarized schematically in Fig. 1(a), started with alternating Ga-Se and In-Se deposition at 330 °C. In the second stage, the temperature was increased to 430 °C, and Cu was evaporated in a Se atmosphere. During this second stage and just before the thin films reached the Cu-rich composition, one of the samples was removed from the process chamber. For the remaining sample, the second stage was completed, ending with a Cu-rich composition. In the third stage, In and Ga were deposited simultaneously in a Se atmosphere in order to consume the secondary $Cu_{2-x}Se$ phase, which is known to form on top of the CIGSe layer at the end of the second stage. At the end of the third stage, the overall film composition was Cu-poor again. Cu deficiency is of importance for highest conversion efficiencies.[18]

Cross-sectional thin lamellas for STEM investigations were prepared by a focused ion beam (FIB) Zeiss Crossbeam XB 1540 EsB instrument, using the *in-situ* lift-out method.[19] Because of the stringent thickness requirement for analytical TEM measurements, we thinned four separate areas at different depth of the absorber layer. This allowed us to probe structural defects at changing [In]/[Ga] ratio through the whole CIGSe absorber layers (see the depth analysis in the supplementary material).

The Zeiss Sub-Electron-Volt Sub-Angstrom Microscope (SESAM) microscope operating at an acceleration voltage of 200 kV was used for STEM-LAADF imaging. The detector angular range was set from 10 to 72 mrad for LAADF imaging, by selecting an appropriate increased microscope camera length to detect electrons that scatter to lower angles than in traditional annular dark-field imaging. Low-angle scattering occurs mainly due to de-channeling of the incident beam in strained regions around defects, thus the LAADF mode allows large-scale imaging of defects in polycrystalline samples.

Before high-resolution STEM (HR-STEM) and EELS analyses a turbo-pumped vacuum oven was used for ex-situ baking of the TEM lamellae and sample holder at 130 °C under 1.33×10^{-4} Pa for 5 h in order to minimize carbon-

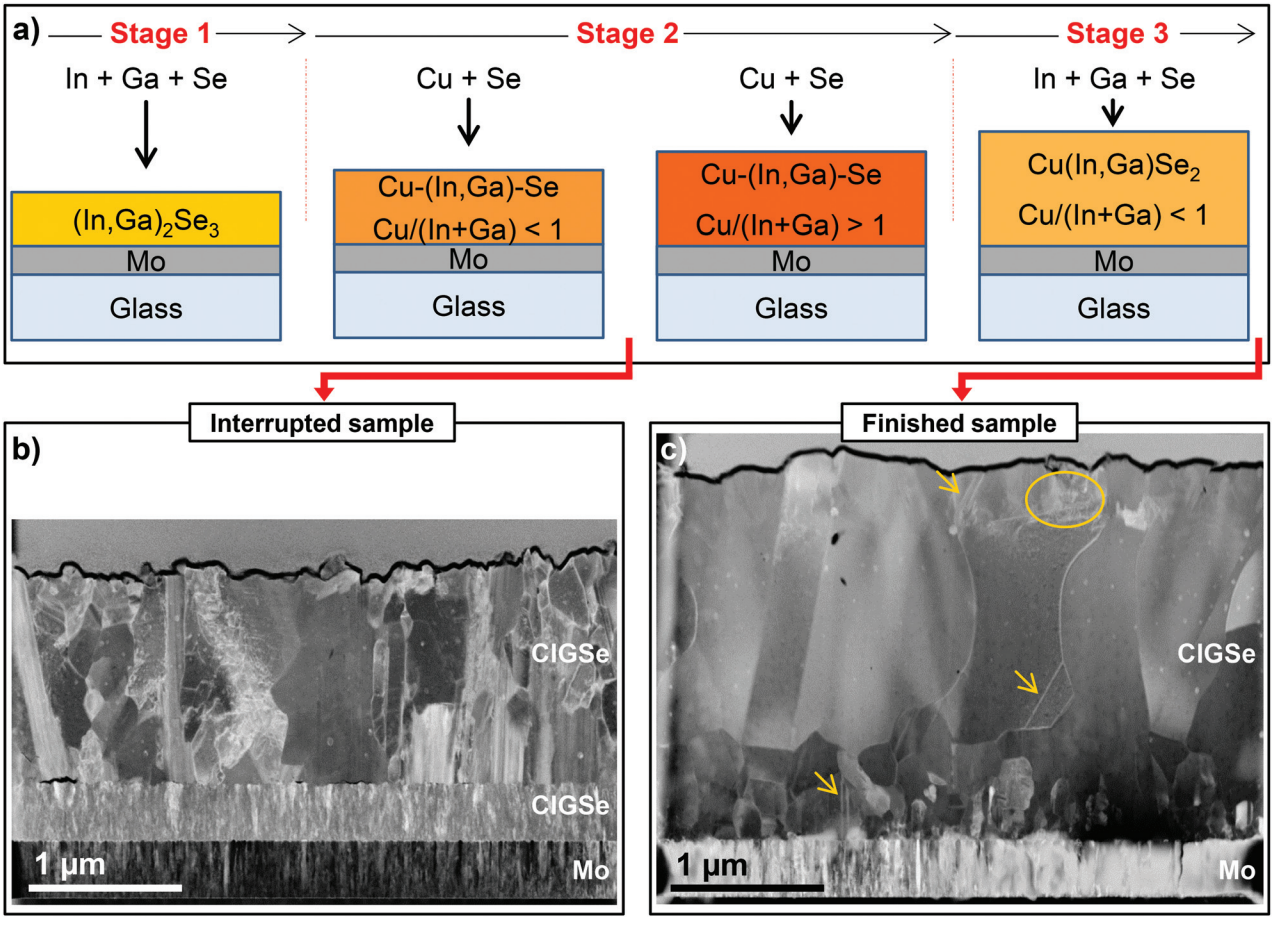

FIG. 1. (a) Schematic drawing of the three-stage-type co-evaporation process. Scanning transmission electron microscopy low-angle annular dark-field images of the Cu-poor (b) interrupted and (c) finished samples.

based contamination. The HR-STEM and EELS measurements were carried out at 100 kV on a Nion UltraSTEM 100 microscope equipped with a cold field emission gun, a Cs corrector and a Gatan Enfina spectrometer. HR-STEM imaging was performed by using simultaneous HAADF and medium-angle annular dark-field (MAADF)/bright field (BF) detectors. The HAADF and MAADF detectors' angular range were set to 85–185 mrad and 42–85, respectively. The BF detector's semi-angle was set to 4.5 mrad. The beam convergence semi-angle was 33 mrad for imaging and the collection semi-angle was 38 mrad for the EELS investigations. The EELS measurements were conducted at 1 eV/channel dispersion covering the energy loss from 315 eV to 1655 eV to allow the simultaneous elemental mapping of In, Cu, Ga, and Se using the In-$M_{4,5}$, Cu-$L_{2,3}$, Ga-$L_{2,3}$, and Se-$L_{2,3}$ ionization edges. The EEL spectra were processed using the Multivariate Statistical Analysis (MSA) plug-in for Gatan Digital Micrograph, based on weighted principal component analysis (PCA), in order to reduce noise.[20]

III. RESULTS AND DISCUSSION

The lower section of the interrupted process sample (Fig. 1(b)), where the composition is Ga-rich and In-poor, shows columnar grains. In the Ga-poor and In-rich top section, the grains are larger in size with a high density of defects, clearly visible from the strain-induced bright contrast of these features in the LAADF images. In contrast, in the finished sample (Fig. 1(c)), the columnar structure at the bottom of the film has clearly disappeared (grains are larger than in the columnar structure, i.e., they have grown). Furthermore, the defect density in the finished sample is much lower, although remaining defects in the grains are still visible in the LAADF images (shown in Fig. 1(c) with yellow marks).

To gain insights into the nature of the defects, high-resolution HAADF imaging was used to observe individual defects at atomic resolution along the ⟨110⟩ projection. In this projection, the CIGSe crystal lattice shows dumbbells formed by closely spaced pure Se^{2-} and alternating In^{3+}/Ga^{3+} trivalent and Cu^{+} monovalent cation columns (Fig. 2). To a good approximation, the intensity of STEM HAADF images is proportional to $Z^{1.7}$, where Z is the average atomic number of the atomic column.[21] However, the simultaneous presence of Cu and In/Ga cations in the same atomic column for ⟨110⟩ zone axis orientation makes distinguishing between column type from images alone challenging. In this case, EELS spectrum image acquisition enables us to identify atom column compositions from selected regions of a sample. An example of a defect-free area is shown in Fig. 2. Note that the intensities on the elemental maps are normalized to a range from 0 to 1 for simplicity, therefore should, not be interpreted in terms of absolute sample compositions. The position of the Se and cation columns are summarised for visual clarity in a composite image displaying a superposition of the Cu, In, Ga, and Se elemental distribution maps. This approach proved to be particularly helpful in elucidating the structure and chemistry of individual structural defects in CIGSe.

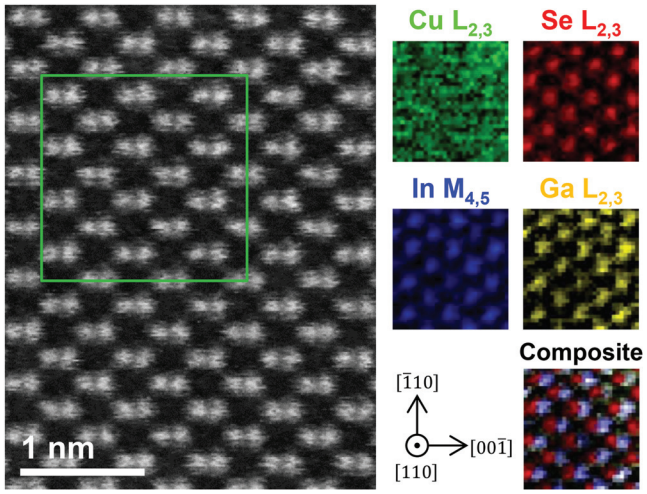

FIG. 2. High-angle annular dark-field image of a defect-free CIGSe lattice along the [110] projection. Cu, In, Ga, and Se elemental distribution maps and the composite image, formed by superimposing the elemental maps, are shown.

A. Structural defects in both samples

The vast majority of defects appeared to be the same in the two samples in terms of structure and composition. The defects appeared to be distributed homogeneously across the absorber layers. The defects shown in the following are from the middle part of the FIB lamellas. Two planar defects—a TB and a "random" GB (i.e., not corresponding to any specific GB with high number of coincident sites)—observed in the interrupted sample are shown in Fig. 3(a) (identical examples of a TB and a GB in the finished sample are shown in the supplementary material). In Fig. 3(a), the upper grain is oriented in ⟨110⟩ direction, whereas the bottom grain is oriented in an unknown direction. Therefore, it is not possible to resolve the atomic columns on both sides of the GB simultaneously. Cu, In, and Se elemental maps (Figs. 3(b)–3(d)), extracted from the EEL spectrum image acquired from the region indicated with a box in Fig. 3(a), show the chemical distribution around the TB and the GB. Fig. 3(e) shows a simultaneous HAADF image and a superimposed red-green-blue (RGB) image for visual conciseness.

These spatially resolved EELS results show a homogeneous elemental distribution at the TB. The cation-Se termination on {112} planes at the TB is depicted by red (Se) and black (cation) circles overlaid on the HAADF image (Fig. 3(a)). The formation mechanism of Se-cation terminated TBs is a 250° (=70° + 180°) rotation around the ⟨110⟩ axis. A similar type of coherent twin boundary is explained in detail for the sphalerite structure by Holt and Yacobi.[22] It was described as an upright (ortho) TB. Due to the correct sequence of cation-Se bonds at this boundary, the interplanar distances remain the same as in the grain interiors. The TB is a special type of Σ boundaries (Σ3).[23] They are the most-frequently found boundaries in CIGSe absorber layers due to their low formation energies. Extensive work has been performed experimentally and theoretically on Σ3 {112} TBs. It has been found that cation-Se-terminated Σ3 TBs do not affect the solar cell properties,[15] a conclusion which seems to be consistent with the lack of any chemical or structural

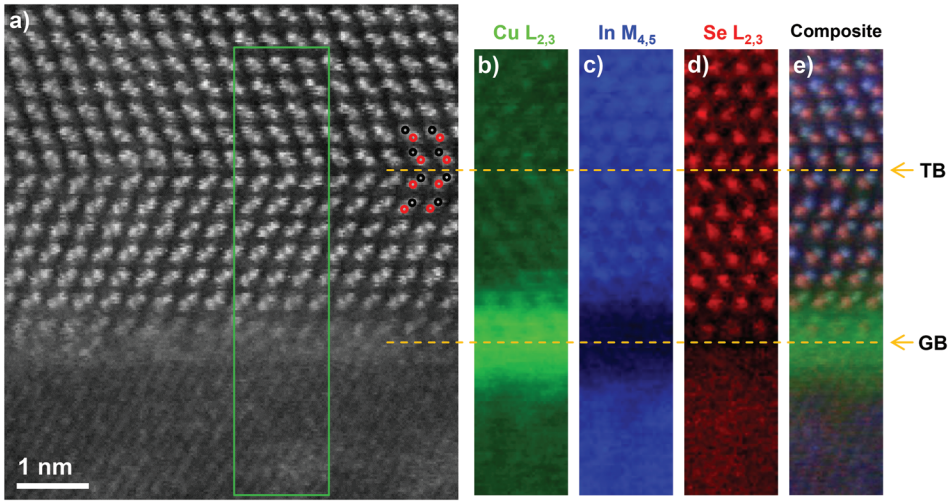

FIG. 3. (a) High-angle annular dark-field image of a Se-cation terminated twin boundary and a random grain boundary from the interrupted sample. The upper grain is oriented in ⟨110⟩ direction. (b)–(d) Elemental distribution maps extracted from the electron energy-loss spectrum image, showing the integrated Cu-$L_{2,3}$, In-$M_{4,5}$, and Se-$L_{2,3}$ intensities, respectively. (e) Red-green-blue composite image, a color-coded combination of elemental distribution maps, superimposed onto the simultaneously acquired HAADF image.

change observed here at atomic resolution. The only possible effect might arise in the case of a close proximity of a large number of such planar faults, which could result in a change in local structure, as was explained for CdTe thin-film solar cells.[24]

In contrast, at the GB a clear chemical change was detected at the cation positions (Figs. 3(b) and 3(c)). The Cu enrichment at the GB region is an indication of the presence of Cu_{In} antisite defects. Cu-rich cation columns (with a large number of such antisite defects) can be found in the terminating layers of the upper grain. At the final plane of the upper grain, slight Se depletion is visible. Careful examination suggests the presence of an increase in oxygen at the GB, although this finding remains ambiguous owing to the overlap of the In-M and O-K edges in the EEL spectra. We did not detect any signal which may be attributed to Na impurities, as expected since a Na-diffusion barrier was deposited between the SLG and the Mo back contact.

Higher Cu diffusion along the GBs than within the grain interiors[3] may be regarded as a reason for the detected Cu enrichment at the GBs, even in the interrupted CIGSe layer, which at no point during the co-evaporation process exhibited a Cu-rich composition. In the finished sample, however, the last deposition stage was In-Ga-Se. The reason for Cu enrichment and In depletion at the GBs in this case may be the compensation of a slight Se depletion.

Less frequent, although found in both investigated samples, are tilt boundaries. Fig. 4 shows a tilt boundary with 113° rotation along the ⟨110⟩ axis (a similar tilt boundary with 105° rotation angle from the finished sample can be seen in the supplementary material). Se exhibits a relatively homogeneous distribution at the boundary. Few darker Se columns at the GB, which can be interpreted as Se vacancies, probably (in part) occupied by oxygen atoms, are visible. Although we are not able to confirm unambiguously the presence of oxygen, previous experimental studies on random GBs by means of atom-probe tomography[25] confirmed increased oxygen concentrations at random GBs, whenever a reduced Se signal was detected.

We found very similar chemical segregation behavior at dislocation cores, i.e., twin-terminated edge dislocations. An overview of two dislocation cores and three Σ3 (112) TBs terminating at the dislocation cores is shown in Fig. 5(a). Averaged sequential imaging (whereby a series of rapidly scanned images is aligned and averaged using rigid registration techniques) was used to obtain images with high signal-to-noise ratio of the two dislocation cores indicated on the overview image with yellow and purple boxes (Figs. 5(b) and 5(f)). As before, EELS analysis revealed that the stoichiometric composition is preserved at and across the Σ3 (112) TBs, while an atomic redistribution of Cu and In is observed at the dislocation cores. This finding is illustrated in Figs. 5(c)–5(e) with elemental distribution maps for Cu, In, and Se at the upper dislocation core, and in Figs. 5(g)–5(i) with the Cu, In, Se maps from the bottom dislocation core. Cu_{In} antisites were found at both dislocation cores.

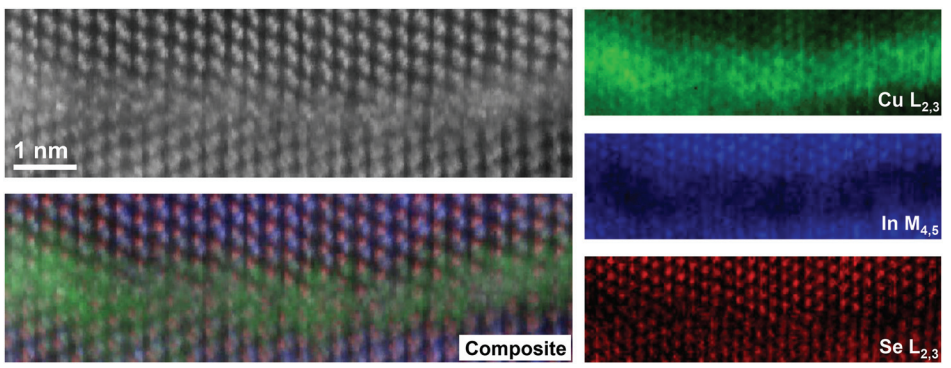

FIG. 4. Simultaneously acquired high-angle annular dark-field image of a tilt boundary. Cu, In, and Se elemental distribution maps from the interrupted sample. The red-green-blue composite image is superimposed on the simultaneous HAADF image.

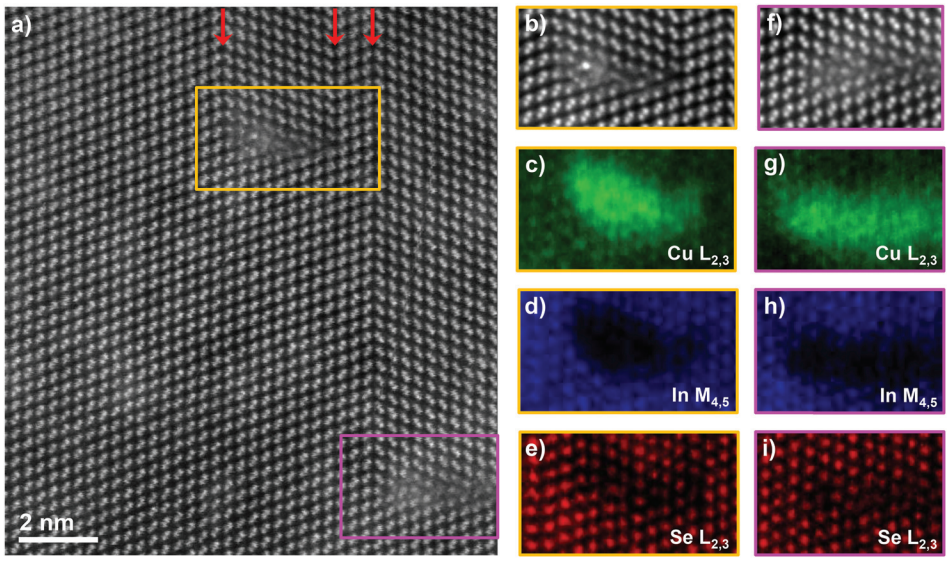

FIG. 5. (a) High-angle annular dark-field image of two dislocation cores with associated twin boundaries from the interrupted sample. (b) and (f) Averaged sequential images of the upper and bottom dislocation cores as it is indicated on Fig. 5(a) by yellow and purple boxes, respectively. (c)–(e) Elemental distribution maps from the upper dislocation core including two twin boundaries. (g)–(i) Elemental distribution maps from the bottom dislocation core and associated twin boundary.

B. Specific structural defects in the interrupted sample

In addition to the line and planar defects described above, we identified inversion boundaries and a number of SF-like complex defects, albeit only in the interrupted process sample. A Se–Se-terminated inversion boundary is found in the interrupted sample (Fig. 6). Unlike in the case of the Se-cation-terminated TBs, due to the Se–Se termination of this defect, the distance between the {112} planes is larger ($d_{112} = 0.48$ nm) than in the grain interiors ($d_{112} = 0.33$ nm), which results in a dark line in the HAADF image (Fig. 6). EEL spectrum imaging confirms the assignment of the terminating ions as Se, the polarity of the Se-cation dumbbell becoming inverted when crossing the boundary. This is illustrated in the composite image where the red columns corresponding to Se are on the right side of the dumbbell in the leftmost section of the image, but on the left side of the dumbbell when crossing the boundary. The distance between terminating columns on either side of the boundary is measured in the HAADF image of Fig. 6 as 0.37 nm, which compares very favorably to the calculated Se-Se distance of 0.35 nm for $CuInSe_2$.[15] At this type of boundary, although the stoichiometric composition is preserved, strong atomic reconstruction is expected, due to the unusual Se–Se "inverted" bonds, which, create Se-dangling bonds. Indeed, the Se–Se termination at the boundary region creates negative excess charge, which in turn might change the local band structure and could alter the absorber properties.

Figs. 7 and 8 show HAADF images and EELS elemental distribution maps acquired on two complex defects. It was found that both defects have the overall characteristics of an intrinsic SF with one missing plane in the ⟨221⟩ direction. Both defects are formed on the {112} planes, although they possess clear structural differences. The defect depicted in Fig. 7 has a similar structure to the inversion boundary; however, atomic reconstruction (Cu enrichment) is induced by

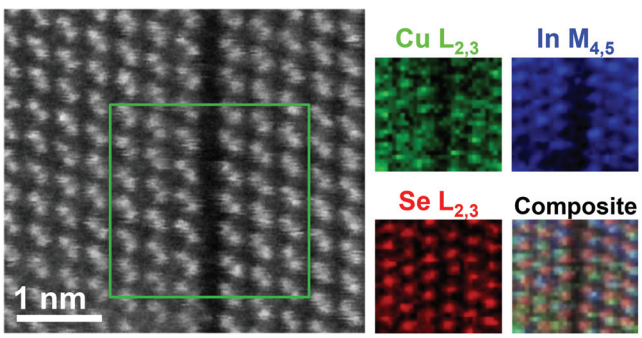

FIG. 6. High-angle annular dark-field image of a Se–Se terminated inversion boundary and the Cu, In, and Se distribution maps extracted from the area indicated with a green rectangle on the high-angle annular dark-field image. The simultaneous HAADF and the superimposed red-green-blue images show a homogeneous elemental distribution. This defect type was observed only in the interrupted sample.

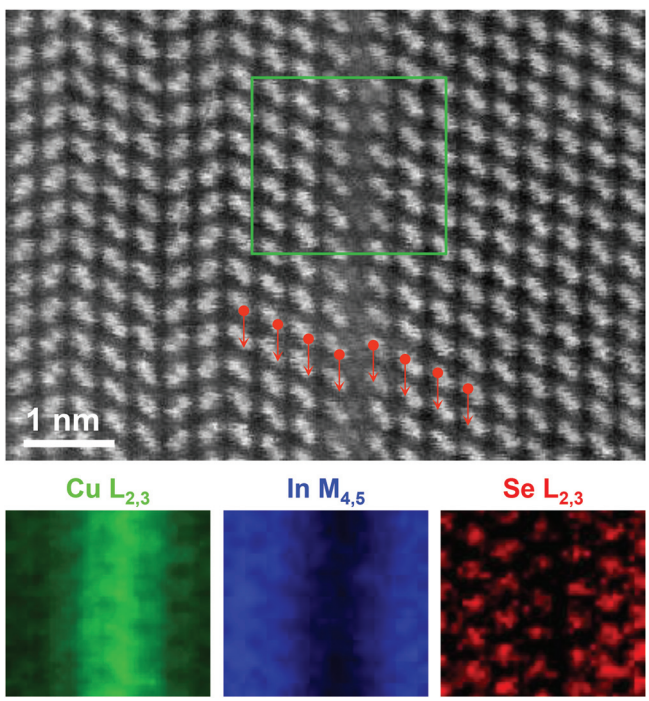

FIG. 7. High-angle annular dark-field image of a stacking-fault-like complex defect from the interrupted sample. Corresponding Cu, In, and Se elemental maps from the denoted rectangle in the HAADF image. Red ball-arrow model shows Se columns across the defect region.

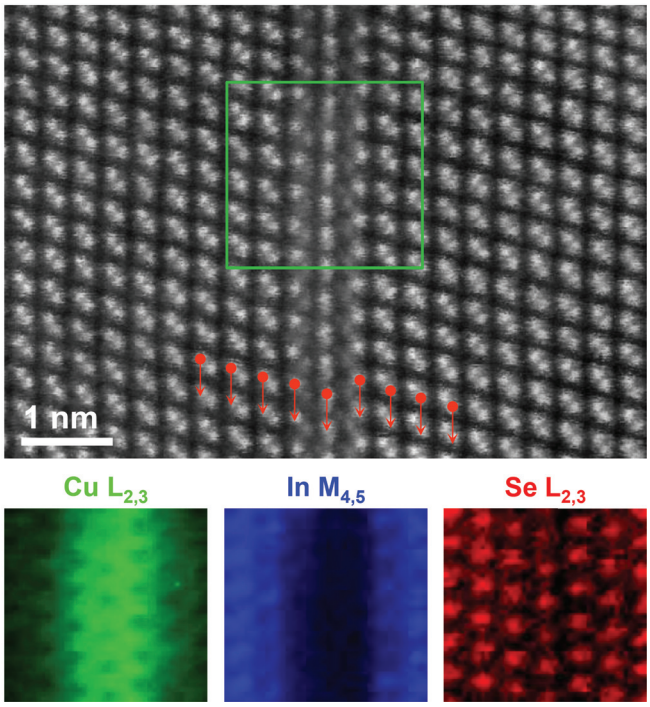

FIG. 8. High-angle annular dark-field image of stacking-fault-like complex defect and corresponding Cu, In, and Se elemental maps from the denoted rectangle in the HAADF image. This defect type was only seen in the interrupted sample. Red ball-arrow model shows Se columns across the defect region.

the Se dangling bonds, thus, helping to reduce the negative excess charge at the defect region. Fig. 8 shows a related structure which includes a rotation of the cation (projected) site within the central plane and for which the planar distances between Se sites (the assignment of which was determined by EELS mapping) are preserved across the defected region.

In both structures, the EELS maps demonstrate how the concentrations of Cu and In vary in an anti-correlated manner, while the Se distribution remains basically homogeneous. As before, the Se maps show slightly weaker intensity at the core of the defect suggesting a possible weak depletion in Se, although channelling effects may also play a role in generating this kind of contrast.

SF-like complex defects might be the indicator of the initial stage of the $Cu_{2-x}Se$ phase, a secondary phase defect occasionally observed in the finished sample. The $Cu_{2-x}Se$ phase exists as a coherent separate phase in the grain also at the GBs, and will be analyzed in more detail in a separate study.

IV. CONCLUSIONS

In conclusion, we studied the microstructural evolution of the structural defects present in Cu-poor CIGSe thin films and provided an overview of their chemical nature. Comparing the microstructure of growth-interrupted and finished Cu-poor CIGSe thin films suggests that grain growth and defect annihilation occurred during the Cu-rich stage of the three-stage-type co-evaporation process. Grain growth in combination with recrystallization was proposed as a defect annihilation mechanism in the CIGSe absorber layers.[6] Except for inversion boundaries and two complex defects detected solely in the interrupted sample, dislocation cores and lattice planes at planar defects were found to be reconstructed atomically in a similar manner for both samples. A stoichiometric composition was measured at highly symmetric defects, i.e., TBs. In contrast, lower symmetry GBs and dislocation cores exhibit a substantial redistribution of Cu and In, i.e., Cu enrichment versus In depletion.

SUPPLEMENTARY MATERIAL

See supplementary material for the STEM energy-dispersive X-ray spectroscopy line-scan results of the growth-interrupted and finished samples. We also show STEM-EELS analysis of a TB, a GB and a tilt boundary from the finished sample.

ACKNOWLEDGMENTS

The authors thank Dr. Bernhard Fenk for FIB sample preparation and Dr. Dieter Greiner for support at the deposition chamber. The work was supported in part by the Helmholtz Virtual Institute HVI-520 "Microstructure Control for Thin-Film Solar Cells", by the European Union Seventh Framework Program [FP/2007-2013] under Grant Agreement No. 312483 (ESTEEM2), as well as by the European Metrology Research Programme (EMRP) Project IND07 Thin Films. The EMRP is jointly funded by the EMRP participating countries within EURAMET and the European Union. SuperSTEM is the UK National Facility for Aberration-Corrected STEM, funded by EPSRC.

[1]P. Jackson, R. Wuerz, D. Hariskos, E. Lotter, W. Witte, and M. Powalla, Physica Status Solidi (RRL) **10**(8), 583 (2016).
[2]T. Schlenker, M. L. Valero, H. W. Schock, and J. H. Werner, J. Cryst. Growth **264**(1–3), 178 (2004).
[3]N. Barreau, T. Painchaud, F. Couzinié-Devy, L. Arzel, and J. Kessler, Acta Mater. **58**(17), 5572 (2010).
[4]H. Stange, S. Brunken, H. Hempel, H. Rodriguez-Alvarez, N. Schäfer, D. Greiner, A. Scheu, J. Lauche, C. A. Kaufmann, T. Unold, D. Abou-Ras, and R. Mainz, Appl. Phys. Lett. **107**(15), 152103 (2015).
[5]R. Caballero, C. A. Kaufmann, V. Efimova, T. Rissom, V. Hoffmann, and H. W. Schock, Prog. Photovoltaics: Res. Appl. **21**(1), 30 (2013).
[6]R. Mainz, E. Simsek Sanli, H. Stange, D. Azulay, S. Brunken, D. Greiner, S. Hajaj, M. D. Heinemann, C. A. Kaufmann, M. Klaus, Q. M. Ramasse, H. Rodriguez-Alvarez, A. Weber, I. Balberg, O. Millo, P. A. van Aken, and D. Abou-Ras, Energy Environ. Sci. **9**(5), 1818 (2016).
[7]H. Rodriguez-Alvarez, N. Barreau, C. A. Kaufmann, A. Weber, M. Klaus, T. Painchaud, H. W. Schock, and R. Mainz, Acta Mater. **61**(12), 4347 (2013).
[8]H. Rodriguez-Alvarez, R. Mainz, B. Marsen, D. Abou-Ras, and H. W. Schock, J. Appl. Crystallogr. **43**(5), 1053 (2010).
[9]Y. Yan, K. M. Jones, J. AbuShama, M. M. Al-Jassim, and R. Noufi, MRS Online Proc. Libr. **668**, H6.10.1 (2001).
[10]S. Nishiwaki, T. Satoh, S. Hayashi, Y. Hashimoto, T. Negami, and T. Wada, J. Mater. Res. **14**(12), 4514 (1999).
[11]D. Abou-Ras, B. Schaffer, M. Schaffer, S. S. Schmidt, R. Caballero, and T. Unold, Phys. Rev. Lett. **108**(7), 075502 (2012).
[12]J. Dietrich, D. Abou-Ras, S. S. Schmidt, T. Rissom, T. Unold, O. Cojocaru-Mirédin, T. Niermann, M. Lehmann, C. T. Koch, and C. Boit, J. Appl. Phys. **115**(10), 103507 (2014).
[13]Y. Yan, W.-J. Yin, Y. Wu, T. Shi, N. R. Paudel, C. Li, J. Poplawsky, Z. Wang, J. Moseley, H. Guthrey, H. Moutinho, S. J. Pennycook, and M. M. Al-Jassim, J. Appl. Phys. **117**(11), 112807 (2015).
[14]D. Abou-Ras, S. S. Schmidt, N. Schäfer, J. Kavalakkatt, T. Rissom, T. Unold, R. Mainz, A. Weber, T. Kirchartz, E. Simsek Sanli, P. A. van

Aken, Q. M. Ramasse, H.-J. Kleebe, D. Azulay, I. Balberg, O. Millo, O. Cojocaru-Mirédin, D. Barragan-Yani, K. Albe, J. Haarstrich, and C. Ronning, Phys. Status Solidi (RRL) **10**(5), 363 (2016).
[15]H. Mirhosseini, J. Kiss, and C. Felser, Phys. Rev. Appl. **4**(6), 064005 (2015).
[16]Z. Yu, D. A. Muller, and J. Silcox, J. Appl. Phys. **95**(7), 3362 (2004).
[17]A. M. Gabor, J. R. Tuttle, D. S. Albin, M. A. Contreras, R. Noufi, and A. M. Hermann, Appl. Phys. Lett. **65**(2), 198 (1994).
[18]M. Kemell, M. Ritala, and M. Leskelä, Crit. Rev. Solid State Mater. Sci. **30**(1), 1 (2005).
[19]M. H. F. Overwijk, F. C. van den Heuvel, and C. W. T. Bulle-Lieuwma, J. Vacuum Sci. Technol. B **11**(6), 2021 (1993).
[20]E. O. Masashi Watanabe and K. Ishizuka, Microsc. Anal. **23**(7), 5 (2009).
[21]D. B. Williams and C. B. Carter, *Transmission Electron Microscopy: A Textbook for Materials Science. Diffraction. II*. (Springer, 1996).
[22]D. B. Holt and B. G. Yacobi, *Extended Defects in Semiconductors* (Cambridge University Press, 2007).
[23]W. Bollmann, *Crystal Defects and Crystalline Interfaces* (Springer-Verlag, 1970).
[24]Y. Yan, K. M. Jones, C. S. Jiang, X. Z. Wu, R. Noufi, and M. M. Al-Jassim, Physica B: Condens. Matter **401–402**, 25 (2007).
[25]D. Abou-Ras, S. S. Schmidt, R. Caballero, T. Unold, H.-W. Schock, C. T. Koch, B. Schaffer, M. Schaffer, P.-P. Choi, and O. Cojocaru-Mirédin, Adv. Energy Mater. **2**(8), 992 (2012).